Polymer 50 (2009) 2696–2705

Contents lists available at ScienceDirect

Polymer

journal homepage: www.elsevier.com/locate/polymer

Time-resolved SAXS studies of self-assembling process of palladium nanoparticles in templates of polystyrene-*block*-polyisoprene melt: Effects of reaction fields on the self-assembly

Yue Zhao [a,b], Kenji Saijo [b], Mikihito Takenaka [b], Satoshi Koizumi [a], Takeji Hashimoto [a,b,*]

[a] *Advanced Science Research Center (ASRC), Japan Atomic Energy Agency (JAEA), Tokai-mura, Ibaraki 319-1195, Japan*
[b] *Department of Polymer Chemistry, Graduate School of Engineering, Kyoto University, Kyoto 615-8510, Japan*

ARTICLE INFO

Article history:
Received 30 January 2009
Received in revised form
3 April 2009
Accepted 8 April 2009
Available online 16 April 2009

Keywords:
Time-resolved SAXS
Self-assembly of nanoparticles
Order–disorder transition

ABSTRACT

Nanocomposites composed of palladium (Pd) nanoparticles, $(Pd)_n$, and a symmetric diblock copolymer (dibcp) of poly(styrene)-*block*-poly(isoprene) (PS-*b*-PI) were prepared via thermal reduction of palladium acetylacetonate, $Pd(acac)_2$, by isothermal heat treatments of the as-cast dibcp films containing $Pd(acac)_2$ by 1 wt%, at temperatures below and above the order–disorder transition temperature (T_{ODT}) of the dibcp. Effects of the reaction field on the thermal reduction process of $Pd(acac)_2$ were studied by setting the field either in the disordered state or the ordered state of the dibcp. The reduction process was studied *in situ* and at real time by time-resolved small-angle X-ray scattering. In the as-cast films, a larger fraction of $Pd(acac)_2$ is preferentially incorporated in PS lamellar microdomains, seemingly due to stronger interactions of $Pd(acac)_2$ with PS than with PI. The spatial concentration fluctuations of $(Pd)_n$ in the final stage of the reduction reflect the memory of the concentration fluctuations of the dibcp before the reduction, either in the disordered state or in the ordered state. We found that the scaled scattering form factor of $(Pd)_n$ is universal with time and temperature of the reduction. This reveals that the reduction mechanism of $Pd(acac)_2$ and the growth mechanism of $(Pd)_n$ do not depend on temperature; they are same below and above T_{ODT}. However, the reduction rate and the growth rate as well as the concentration of $(Pd)_n$ in the final stage depend on temperature: the higher the temperature is, the larger are the rate and the concentration.

1. Introduction

In the past decades, the block copolymers (bcps) based materials have attracted much attention from both industrial and academic view points, because they developed well-ordered multiphase structures with nano-scale periodicity and can be used to create nano-patterned materials [1–3]. Most of the early studies focused on pure organic polymers in terms of their phase behavior and their dynamics [4–6]. Recently, bcps with solid fillers have been widely used to produce high-performance materials, as they offer very unique mechanical and physical properties, i.e., high strength, high modulus, high heat distortion temperatures, and etc. [7–9]. Another exciting example is that the self-assembling bcps with metal nanoparticles could hold characteristic electronic, magnetic, and photonic properties [10–15], which may lead to a new generation of materials.

Various methods have been reported to obtain the metal nanoparticles selectively incorporated within one of the microdomains of bcps. The synthetic approach involves the reduction of the organometallic bcps, which have metal-complexes chemically linked to one of block chains, to yield metal nanoparticles in one of the microdomains of bcps [16–19]. The incorporation approach involves a selective loading of metal-complexes in one of the microdomains by using selective physical interactions of them with block chains and a subsequent chemical or thermal reduction of the metal-complexes [20–23]. For example, Saito et al. introduced silver colloids into the cross-linked poly(2-vinylpyridine) (P2VP) domains of polystyrene (PS)-*block*-poly(2-vinylpyridine) (PS-*b*-P2VP) by soaking the bcp films in the $AgNO_3$/water/1,4-dioxane solution and by subsequent chemical reduction [20]. Horiuchi et al. presented a dry process involving sublimation of palladium acetylacetonate, $Pd(acac)_2$, vapor onto the bcp films at high temperatures for a certain time, which caused the thermal reduction to Pd(0) atoms followed by an aggregation into Pd nanoparticles, defined hereafter $(Pd)_n$, inside the polymer films [21]. In our previous communication, we introduced a combination of small-angle X-ray scattering (SAXS)

* Corresponding author. Advanced Science Research Center (ASRC), Japan Atomic Energy Agency (JAEA), Tokai-mura, Ibaraki 319-1195, Japan.
E-mail address: hashi2@pearl.ocn.ne.jp (T. Hashimoto).

0032-3861/$ – see front matter © 2009 Elsevier Ltd. All rights reserved.
doi:10.1016/j.polymer.2009.04.013

and transmission electron microscope (TEM) methods to demonstrate $(Pd)_n$ formed selectively in poly(2-vinylpyridine) (P2VP) domains of polyisoprene(PI)-*block*-poly(2-vinylpyridine) (PI-*b*-P2VP) by reducing $Pd(acac)_2$ in the lamellar microdomain space developed in the concentrated polymer solution with benzyl alcohol, where benzyl alcohol worked as a solvent and a reducing agent [22]. Lately, Sakamoto et al. [23] reported time-resolved SAXS measurements to study the kinetics of this reaction-induced self-assembling process of $(Pd)_n$ in the swollen lamellar microdomain space, and they pointed out that the final size and total volume of $(Pd)_n$ grown in the microdomain space depend on the reduction temperature.

The observations of metal nanoparticles created by the reduction of metal-complexes or ions have been conducted mainly by TEM [19–22,24–26], wide-angle X-ray scattering (WAXS) [19,27] and SAXS [19,22,23,28,29]. However, the TEM analysis is not suitable for *in situ* observation of formation processes of metal particles. By WAXS, we cannot detect the real-size of metal nanoparticles, if they consist of polycrystals.

Up to now, except for the studies of Sakamoto et al. [23], the SAXS measurements were performed only before and after the reduction, where the measurements during the reduction process were missing. Thus the kinetics of the nanoparticle formation process and mechanisms in the bcp matrices are still not completely understood. The time-resolved SAXS method introduced by Sakamoto et al. [23] shed light on *in situ* observation of nanoparticle formation process. In this work also, we shall focus on the kinetics of the reduction-reaction-induced self-assembling process of $(Pd)_n$ in polystyrene-*block*-polyisoprene (PS-*b*-PI) bcp matrix by time-resolved SAXS. Comparing with the work by Sakamoto et al., the merits of this study are as follows: i) The reduction is performed in the polymer melt by a heat treatment, so that no extra reducing agent is introduced in the system; ii) The order–disorder transition (ODT) temperature (T_{ODT}) window of the PS-*b*-PI bcp used in this study is between 159 °C and 161 °C. Therefore, it is easy to manipulate the reduction reaction both in the ordered state below T_{ODT} of the bcp and in the disordered state above T_{ODT}, so that we can study effects of the reduction field (the disordered state or ordered state) on the reduction reaction of $Pd(acac)_2$ into palladium atoms, Pd(0), and the aggregation process of Pd(0) into $(Pd)_n$; iii) After the completion of the reduction, the T_{ODT} window of the nanocomposites is still measurable, if it exists, enabling us to study effects of $(Pd)_n$ on ODT of the nanocomposites.

2. Experimental section

2.1. Sample preparations

PS-*b*-PI ($M_n = 2.15 \times 10^4$, $M_w/M_n = 1.02$, and the volume fraction of PS, $f_{PS} = 0.55$) was synthesized by living anionic polymerization with *sec*-butyl-lithium as an initiator and cyclohexane as a solvent. Neat bcp films and films containing $Pd(acac)_2$ by 1 wt% were prepared by first dissolving a prescribed amount of PS-*b*-PI (4.95 wt%) without or with $Pd(acac)_2$ (0.05 wt%) in benzene and then slowly evaporating the solvent. The evaporation was carried out at room temperature in air for one week and then in a vacuum oven for three days.

2.2. SAXS measurements

The SAXS profiles were measured *in situ* with the SAXS apparatus described elsewhere [30]. The profiles were corrected for absorption, air scattering, background scattering arising from thermal diffuse scattering (TDS), and slit-height and slit-width smearing. To reduce the possible thermal degradation, the sample chamber was filled with nitrogen gas, and the temperature was controlled with an accuracy of ±0.003 °C.

The ODT measurements for the neat PS-*b*-PI film started from 180 °C. A well-designed cooling–heating cycle was implemented, and the SAXS measurements were done at 1° temperature increments or decrements across T_{ODT}. At a given temperature the sample was held for about 30 min before the SAXS measurement with a measuring time of 30 min; Then the measuring temperature is shifted up or down to the next temperature where the SAXS measurement was repeated in the same way as described above. The $Pd(acac)_2$ incorporated in the bcp films was thermally reduced at reduction temperatures, T_rs. T_r was set at 180 °C for the reduction in the disordered bcp melts or at 142 °C for the reduction in the bcp microdomains. Time-resolved SAXS measurements were performed continuously at the respective temperatures with a measuring time of 5 min to explore the effects of the bcp matrices as the reaction fields on the reduction of $Pd(acac)_2$ and formation of $(Pd)_n$.

3. Results

3.1. Determination of T_{ODT} for neat bcp

T_{ODT} for the neat PS-*b*-PI bcp can be determined from the discontinuous change of the first-order SAXS peak with temperature T, in terms of its maximum intensity (I_m), and half width at half maximum (HWHM, σ_q). Conventionally, in the study of ODT, the plot of I_m^{-1} or σ_q^2 vs T^{-1} shows a discontinuous change at a particular temperature, designated T_{ODT} [31–36], as a consequence of thermal fluctuation induced first-order transition [37].

Fig. 1 shows I_m^{-1} and σ_q^2 plotted as a function of T^{-1} for the neat PS-*b*-PI film, in both the cooling and heating cycles. As we expect, both I_m^{-1} and σ_q^2 have a similar temperature dependence. A sharp discontinuity appears in a narrow temperature range between 158 °C and 160 °C in the cooling process and between 159 °C and 161 °C in the heating process. The ordered state coexists with the disordered state in the very narrow temperature range around T_{ODT}, presumably due to thermal fluctuation effects [38]. The variation of I_m^{-1} and σ_q^2 with T^{-1} in the heating and cooling processes reveals that the hysteresis phenomenon is small under the given thermal protocol. This must also imply the fact that the thermal degradation of the bcp could hardly occur during the heating and cooling processes.

3.2. Microdomain structures of as-cast films with and without $Pd(acac)_2$

Fig. 2 shows the typical SAXS profiles for as-cast films of the bcp with and without $Pd(acac)_2$, measured from the edge direction (incident beam parallel to the surfaces of stacked films). The profiles were corrected for thermal diffuse scattering (TDS) due to the acoustic phonons propagating in the specimens by using the method as will be detailed below in conjunction with Fig. 3. Scattering intensity I is plotted in logarithmic scale against the magnitude of the scattering vector, q, where q is defined by $q = (4\pi/\lambda)\sin(\theta/2)$ with $\lambda = 0.154$ nm and θ = scattering angle, respectively. The second- and third-order Bragg peaks are observed at $q = 2q_m$ and $3q_m$, respectively, where q_m is the q value at the first-order scattering maximum, indicating the ordered lamellar microdomain structures were formed for both cases. Though the maximum intensity, I_m, from the $Pd(acac)_2$ containing film (curve 1) is significantly larger than that from the neat bcp film (curve 2), the q_m remained almost the same: $q_m \sim 0.367\ nm^{-1}$, corresponding to a characteristic length D (defined by $D = 2\pi/q_m$) ~ 17 nm. Therefore, the films with and without $Pd(acac)_2$ have the alternating lamellar microdomains rich-in PS blocks and PI blocks, with an almost identical repeat distance.

The fact that the scattering intensity of the $Pd(acac)_2$ containing film is higher than that of the $Pd(acac)_2$ free film reveals that

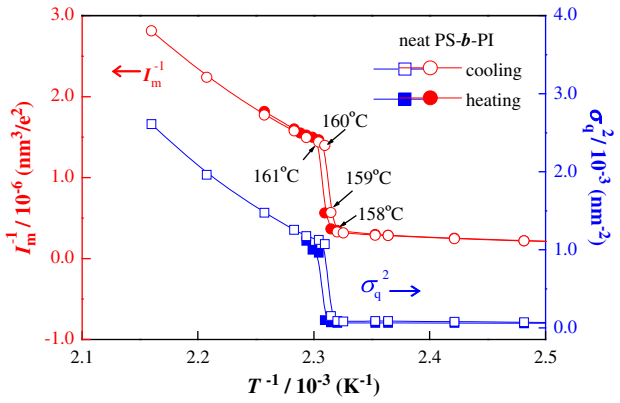

Fig. 1. I_m^{-1} (red lines, symbols, and axis) and σ_q^2 (blue lines, symbols, and axis) plotted as a function of T^{-1} for neat PS-*b*-PI film, in both cooling and heating cycles. Temperatures around T_{ODT} are marked with the arrows. (For interpretation of colour in this figure, the reader is referred to the web version of this article.)

Pd(acac)$_2$ complexes are preferentially incorporated into PS lamellae, hence enhancing the electron density (ρ_{el}) difference ($\Delta\rho_{el}$) between PS and PI lamellae. Note that: ρ_{el} for PS is higher than ρ_{el} for PI; hence the preferential incorporation of Pd(acac)$_2$ having the highest ρ_{el} further increases $\Delta\rho_{el}$ and thereby the scattering intensity. Thus the enhanced intensity provides a firm evidence for the preferential incorporation of Pd(acac)$_2$. The preferential incorporation will be further confirmed later in Section 4.1 in conjunction with the note in Ref. [42]. The smaller peak width (full width at half maximum, FWHM, being 0.012 nm and 0.018 nm for the bcp film containing Pd(acac)$_2$ and the neat bcp films, respectively) or the higher regularity of the lamellae for the Pd(acac)$_2$ containing film may infer a larger effective segregation power between PS and PI domains, which in turn may imply that the T_{ODT} of Pd(acac)$_2$ containing film may be higher than that of the neat PS-*b*-PI bcp. However, systematic ODT measurements of Pd(acac)$_2$ containing film are impossible, because the reduction of Pd(II) occurs fast at $T \geq 60$ °C, which would affect T_{ODT} during the SAXS measurements as a function of *T*.

As for SAXS profiles obtained with the through-direction (with incident beam normal to the film surface, though not shown here), multiple-order peaks were much broader, and the intensities of the first-order peaks were weaker, though the peak positions were similar for both films. It indicates that lamellae in the as-cast films

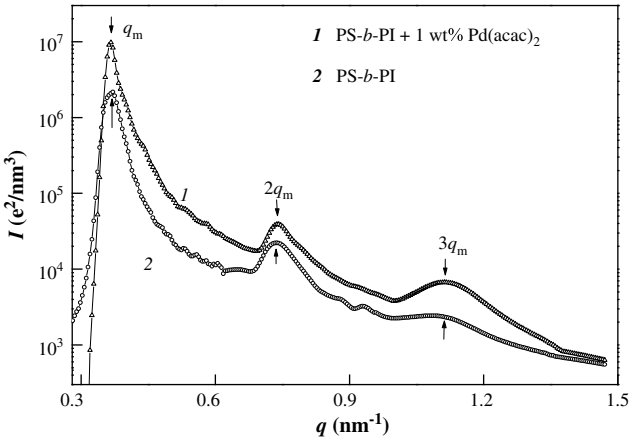

Fig. 2. SAXS profiles for as-cast films of the bcp with and without Pd(acac)$_2$, measured from the edge direction.

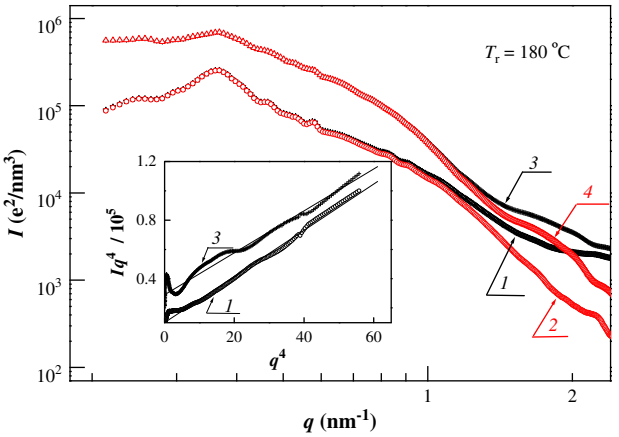

Fig. 3. Two SAXS profiles for the films containing Pd(acac)$_2$, which are reduced at 180 °C for 5 min [curve 1: before the TDS correction (black symbols); curve 2: after the TDS correction (red symbols)] and 180 min [curve 3: before the TDS correction (black symbols); curve 4: after the TDS correction (red symbols)]. The inset figure describes a way to estimate the TDS. (For interpretation of colour in this figure, the reader is referred to the web version of this article.)

were preferentially oriented with their interfaces parallel to the film surfaces (parallel lamellae) and the lamellae with their interfaces oriented perpendicular to the film surfaces were less ordered than the parallel lamellae, the trend of which is well known [39]. Time-resolved SAXS measurements during the reduction process of Pd(acac)$_2$ were performed with the through-direction.

3.3. Reduction of Pd(acac)$_2$ in the disordered bcp

Fig. 3 shows the SAXS profiles taken *in situ* at 180 °C where the reduction takes place in the disordered bcp matrix. The profiles 1 and 3 were measured after 5 min and 180 min reduction, respectively. The profiles 2 and 4 were corrected for TDS from the original profiles 1 and 3, respectively. The inset figure describes a way to estimate the TDS. In principle, the TDS was assumed to be a constant (*b*) independent of *q* in the *q* region covered in this work, while the scattering from internal structures of the specimens at the high *q* region is given by the Porod law [40], $I(q) \propto q^{-4}$. Note here that the scattering is dominated by (Pd)$_n$ with a smooth interface and a sharp interface boundary in the *q* range of the observation. Consequently, the net scattering, $I_{net}(q)$, is given by $I_{net}(q) = aq^{-4} + b$, where *a* is a proportionality constant. Therefore TDS was determined from the slope of Iq^4 vs q^4 plot at the high *q* region, as shown in the inset. After the TDS correction, the intensity kept being dropped with *q* in the high *q* range ($q > 0.9$ nm^{-1}), as shown by the profiles 2 and 4. The TDS correction is important for quantitative estimations of the size and its distribution of (Pd)$_n$, as will be discussed later.

Fig. 4 presents the changes in the SAXS profiles corrected for TDS (shown by symbols) with time, taken *in situ* at 180 °C, during the whole reduction process together with the scattering from the neat bcp film in the disordered state (solid line) taken also at 180 °C as a reference. It is interesting to note that the maximum scattering intensity I_m for the films subjected to the reduction for a short time (e.g. curve 1 for 5 min) is weaker than that for the neat as-cast film. This will be discussed later in Section 4.2.1.

The part a shows the scattering profiles obtained at 7 representative heat-treatment times from 5 to 180 min, some of which are overlapping one another. The profiles in part b were vertically shifted deliberately to avoid overlapping of the profiles in order to illuminate the details of each profile. In part a, a broad peak marked by an arrow is observed at $q \sim 0.37$ nm^{-1} for all the profiles, suggesting the bcp

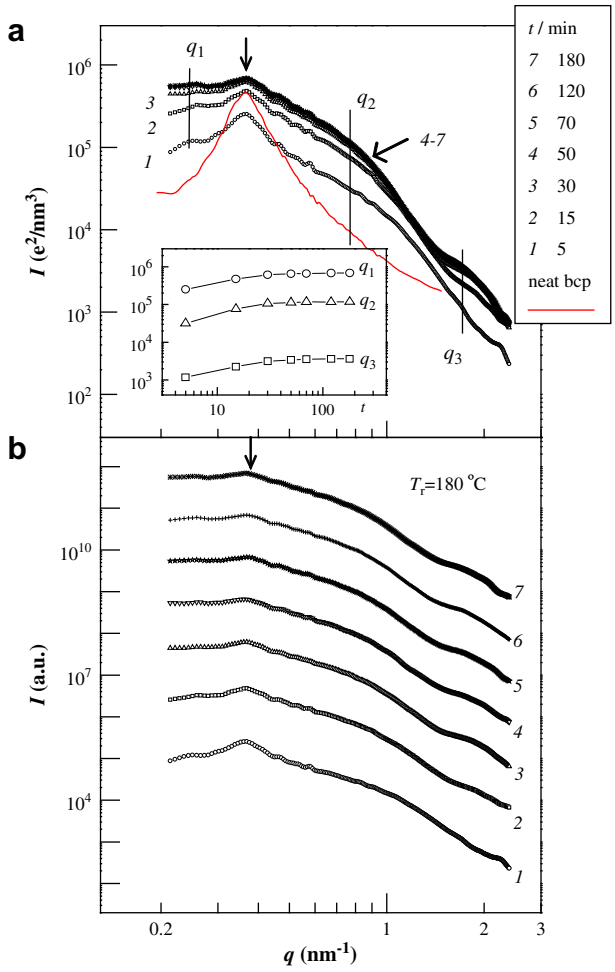

Fig. 4. Time change in the SAXS profiles during the reduction process at 180 °C for the films containing Pd(acac)$_2$. (a) Representative scattering profiles (shown by symbols) obtained at 7 different heat-treatment times from 5 to 180 min. The scattering from the neat bcp film at 180 °C was also shown by a red solid line as a reference. The inset shows the time dependence of intensities at three representative q values, where the x-axis is time in min and y-axis is the absolute intensity in e^2/nm^3. (b) Vertically shifted profiles shown in part (a) to avoid overlapping the profiles. (For interpretation of colour in this figure, the reader is referred to the web version of this article.)

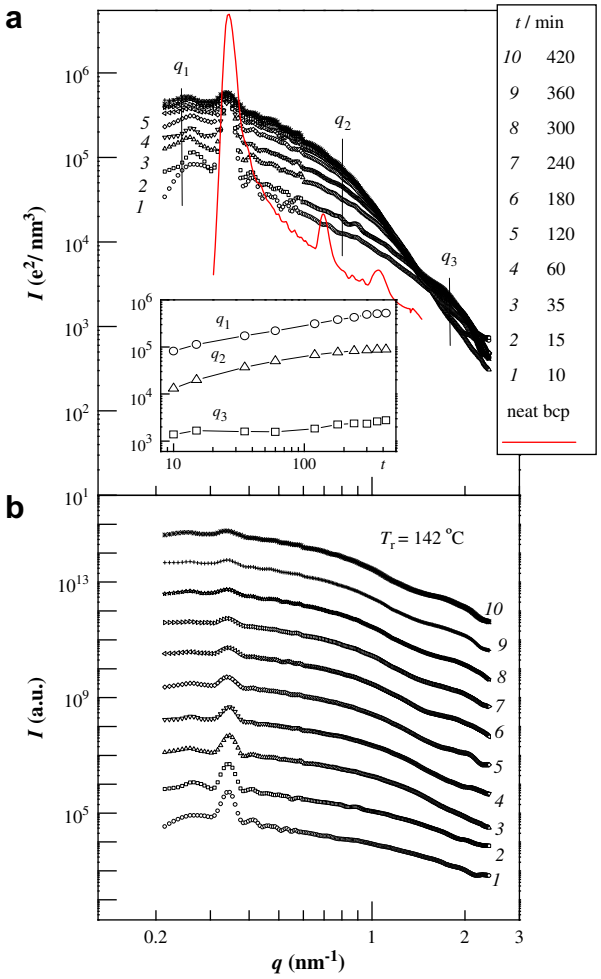

Fig. 5. Time change in the SAXS profiles during the reduction process at 142 °C for the films containing Pd(acac)$_2$. (a) Representative scattering profiles (shown by symbols) obtained at 10 different heat-treatment times from 10 to 420 min. The scattering from the neat bcp film at 142 °C was also shown by a red solid line as a reference. The inset shows the time dependence of intensities at three representative q values, where the x-axis is time in minutes and y-axis is the absolute intensity in e^2/nm^3. (b) Vertically shifted profiles shown in part (a) to avoid overlapping. (For interpretation of colour in this figure, the reader is referred to the web version of this article.)

matrix stays in the disordered state during the whole reduction process. The scattering intensity increases fast within the first 30 min throughout the whole q range, revealing that the reduction of Pd(acac)$_2$ and the formation of the (Pd)$_n$ are fast at 180 °C. Intensities at three representative q values were plotted against time in the inset. The reduction was completed within 120 min, since no further change of the intensities could be found with time.

3.4. Reduction of Pd(acac)$_2$ in the ordered bcp

Fig. 5 shows the change in SAXS profiles with time during the reduction at 142 °C (shown by symbols) together with the profile from the neat bcp film at 142 °C (shown by solid line) as a reference. Similarly to Fig. 4, original and vertically shifted profiles were shown in Fig. 5a and b, respectively. The intensities at the three representative q values were plotted against time in the inset of Fig. 5a. A continuous increase of the intensity with time was observed at each q, indicating the Pd particles were forming gradually over the time scale covered in this experiment. A peak appears always at $q_m = 0.34$ nm^{-1}, corresponding to the first-order peak from the lamellar microdomains having spacing of 18.5 nm. Its intensity I_m and its position q_m remain almost a constant with time t at $t > 10$ min. After 420 min, the profile does not change, and the particle scattering dominates the net scattering which comprises the particle scattering and the scattering from the lamellar microdomains. It is interesting to note here again that I_m for the reduced films is lower than that for the neat bcp film at the same temperature, which will be discussed later in Section 4.2.2.

After the completion of the reduction (180 min at 180 °C and 420 min at 142 °C), SAXS measurements were carried out in a cooling–heating cycle, in order to measure their T_{ODT}s. The results indicated that T_{ODT} is lowered down to 148–144 °C and 158–154 °C for the specimens after the complete reduction at 180 °C and 142 °C, respectively, as will be reported in detail by a companion paper [41].

4. Discussion

4.1. Interactions of Pd(acac)$_2$ with PS and PI block chains

Pd(acac)$_2$ was preferentially incorporated in PS lamellar microdomains, as clarified in Section 3.2 in conjunction with Fig. 2. The

scattering maximum for the films containing $Pd(acac)_2$ is about 4 times stronger than that for the complex free film, partly because $Pd(acac)_2$ containing film is much ordered and partly because $Pd(acac)_2$ is preferentially incorporated in PS lamellae, so that the effective electron density difference between the two lamellar microdomains becomes larger. This is probably because $Pd(acac)_2$ may have a stronger coordination with benzene rings in PS than with double bonds in PI after the evaporation of the casting solvent. This result is consistent with another experiment performed in parallel [42].

4.2. Reduction of $Pd(acac)_2$ in PS-b-PI matrix

4.2.1. Reduction in disordered state

All the profiles in Fig. 4 taken at 180 °C show the broad peak at $q_m \sim 0.37\ nm^{-1}$ even after the reduction for 180 min at 180 °C, indicating that the bcp specimens are in the disordered state from the very beginning to the end of the reduction process at this temperature. The peak intensity, I_m, and the scattering intensity around the peak *decrease* in the first 5 min in comparison with that of the neat bcp at the same temperature, possibly due to a suppression of the thermal concentration fluctuations of the bcp caused by the reduction and formation of $(Pd)_n$ and possibly due to a preferential reduction in the regions rich-in PI blocks compared with the regions rich-in PS blocks as described below.

As we discussed in Section 4.1, $Pd(acac)_2$ has stronger attractions or coordinations with PS blocks than with PI blocks, which results in the reduction of $Pd(acac)_2$ in PS-rich regions being harder and slower than that in the PI-rich regions. Consequently Pd(0) atoms are formed more easily and faster in the PI-rich regions than in the PS-rich regions, because a lower energy barrier is required for the reduction of $Pd(acac)_2$ in PI-rich regions. Moreover, Pd(0) atoms may grow faster into $(Pd)_n$ particles in PI-rich regions than in PS-rich regions. This faster consumption of $Pd(acac)_2$ and Pd(0) atoms in the PI-rich regions may offer a driving force for $Pd(acac)_2$ and Pd(0) atoms in the PS-rich region to diffuse into the PI-rich regions [43]. These effects decrease the net electron density difference, $\Delta\rho_{fluct}$, between PI- and PS-rich regions in the disordered state, which may offer a part of the reason for the suppression of I_m in the early stage of the reduction relative to I_m for the neat bcp at the same temperature (180 °C). The following two factors, (i) $(Pd)_n$ created after the reduction is more or less neutral to both PS and PI blocks and (ii) the reduction of $Pd(acac)_2$ preferentially interacting with PS blocks to Pd(0)s decreases net repulsive interactions between PI blocks and PS blocks, together may offer another reason for the suppression of I_m. However, the intensity in the low q region (at $q < 0.32\ nm^{-1}$) and that in the high q region (at $q > 0.45\ nm^{-1}$) increase even in the early stage at $t = 5$ min, due to a greater contribution of the scattering from $(Pd)_n$ than the contribution of the scattering from the microdomain structure itself in these q ranges.

After 5 min, the scattered intensity increases in the whole q range as clearly shown in Fig. 4a and its inset. This is due to the fact that the number of nanoparticles increases with the reduction time and that the scattering from the nanoparticles dominates over that from the bcps themselves. Nevertheless, the scattering maximum at q_m is conserved till the end of the reduction process, implying that the spatial concentration fluctuations of the nanoparticles replicate the thermal concentration fluctuations in the disordered bcp melts.

4.2.2. Reduction in ordered state

All the profiles from the specimens after the reduction in Fig. 5 show a peak at the same q_m as the peak for the neat bcp, indicating that the specimens are in the ordered state from the very beginning to the end of the reduction process at 142 °C. This result is also confirmed by the fact that the nanocomposite (i.e., the bcp containing nanoparticles) itself exhibited ODT as revealed by a discontinuous change of I_m^{-1} and σ_q^2 with T^{-1} as will be elucidated by a companion paper [41].

The peak intensity, I_m, decreases in comparison with that of the neat bcp at the same temperature, which should be due to a suppression of the net electron density difference between the two domains due to the following reasons. Similarly to what we discussed above in Section 4.2.1, although the reduction of $Pd(acac)_2$ occurs both in PS lamellae and in PI lamellae, the reduction in PS lamellae is harder and slower than that in the PI lamellae. Moreover, Pd(0) atoms grow faster into $(Pd)_n$ particles in the PI lamellae than in the PS lamellae. The faster consumption of $Pd(acac)_2$ and Pd(0) atoms in the PI lamellae may offer a driving force for $Pd(acac)_2$ and Pd(0) atoms in the PS microdomains to diffuse into the PI microdomains [43]. These effects as described above will increase ρ_{el} for PI lamellae relative to that for PS lamellae and hence decrease the net electron density difference, $\Delta\rho_{domain}$, between the PI and PS lamellae, which accounts for the observed decrease in I_m. The formation of $(Pd)_n$ may distort the order in the lamellar microdomains, which may also account for the decrease of I_m. Although the scattered intensity around q_m ($0.32\ nm^{-1} < q < 0.37\ nm^{-1}$) decreases, the intensity in the low q range (at $q < 0.32\ nm^{-1}$) and that in the high q range (at $q > 0.37\ nm^{-1}$) increase, due to the contribution of the scattering from $(Pd)_n$ being greater than that from the lamellar microdomains.

The scattered intensity at $t > 10$ min increases with t in the whole q range as clearly shown in Fig. 5a and its inset. This can be attributed to the fact that the number of nanoparticles increases with the reduction time and that the scattering from the nanoparticles dominates that from the bcp microdomains themselves. The peak position q_m is effectively unaltered with time throughout the reduction process. This is because the increased number of $(Pd)_n$ expands the microdomains in the directions parallel and perpendicular to the interfaces, i.e., the lateral and longitudinal expansions, respectively. On one hand, the longitudinal expansion tends to increase D, and hence decrease q_m; on the other hand, the lateral expansion tends to increase the average distance between the neighbouring junction points of the bcps along the interface and hence to decrease D or increase q_m. The counterbalance of these two contributions may result in the unchanged q_m with time or with the number of $(Pd)_n$.

At 180 °C, most of the $Pd(acac)_2$ was reduced and transformed to $(Pd)_n$ after 50 min. Therefore, no further change was observed later on. However, at a relatively lower temperature, i.e., 142 °C, the visible reduction period was extended up to 420 min.

4.2.3. Scattering from $(Pd)_n$

Because the scattering from $(Pd)_n$ is much stronger than that from concentration fluctuations of bcp themselves in disordered state at 180 °C and that from bcp microdomain structure themselves in the ordered state at 142 °C, and because the inter-nanoparticles interference seems to be negligible at $q > 0.4\ nm^{-1}$, we can employ the independent scattering theory from the nanoparticles to describe our system in the q range of our interest. To investigate the formation of the $(Pd)_n$ during the heat-treatment, the scattering form factor from the solid spheres, $F(q)$, with a Gaussian size distribution is applied to fit the SAXS profiles at $q > 0.4\ nm^{-1}$ shown in Figs. 4 and 5.

The scattering intensity, $I_{sph}(q)$, from a single sphere is given by [44]:

$$I_{sph}(q) = \rho_0^2 v^2 F(q), \quad F(q) = \frac{9(\sin qR - qR\cos qR)^2}{(qR)^6} \tag{1}$$

where $F(q)$ is the form factor of a sphere having radius R, ρ_0 is the electron density difference between the sphere and the surrounding medium, and v is the volume of the sphere, $v = (4/3)\pi R^3$. The average

scattering intensity, $\overline{I_{sph}(q)}$, from a single sphere with a Gaussian size distribution is given by

$$\overline{I_{sph}(q)} = \int_0^\infty I_{sph}(q,R)P(R)\,dR \equiv \rho_0^2 \overline{v^2 F(q)} \quad (2)$$

$$P(R) = (2\pi)^{-1/2}\sigma_R^{-1}\exp\left[\frac{-(R-R_n)^2}{(2\sigma_R^2)}\right] \quad (3)$$

where $P(R)$ is the normalized size distribution function, $R_n = R_n(t,T)$ is the number-average particle radius, which depends on reduction time t and temperature T, and $\sigma_R = \sigma_R(t,T)$ is the standard deviation of R from R_n. Based on Eqs. (2) and (3), we fit the measured scattering profiles at $0.4\ nm^{-1} < q < 2\ nm^{-1}$ with the theoretical scattering function numerically calculated from Eqs. (2) and (3). The inset of Fig. 6 demonstrates a representative fitting result for the reduction at 180 °C for 180 min: both the measured scattering profile (symbols) and the best-fitted theoretical profile (red solid line) are shown together with $P(R)$. We determine the steady-state values of R_n and σ_R/R_n from the best fitting: $R_n \sim 2.7$ nm, and $\sigma_R/R_n \sim 0.26$ at 180 °C for 180 min.

The characteristic parameters R_n and σ_R/R_n thus evaluated are plotted as a function of time in Fig. 6. R_n and σ_R/R_n rapidly increases and decreases, respectively, with time for the first 30 min and then both of them gradually approaches the steady values. It indicates that on one hand, $(Pd)_n$ is formed and grows into a larger size in the polymer matrix according to the mechanisms suggested by the previous report [45]; on the other hand, the particle size distribution narrows.

The same analysis was carried out for the scattering profiles shown in Fig. 5 (at 142 °C). The time dependence of thus determined R_n and that of σ_R/R_n are plotted in Fig. 7. It shows that at 142 °C, both R_n and σ_R/R_n change gradually with time toward steady values at $t \geq 350$ min. The inset shows both the measured scattering profile (shown by symbols) and the best-fitted theoretical profile (shown by red solid line) for the specimen after the reduction at 142 °C for 420 min as a typical example of the fitting result. One can read the steady values of $R_n \sim 2.7$ nm and $\sigma_R/R_n \sim 0.27$ at 142 °C for 420 min. Note that the particle size and size distribution at the final reduction state are very similar at both T_rs, which indicates the final size and size distribution of the $(Pd)_n$ are T-independent, they are intrinsically controlled by the nature of the bcp matrix. Here it should be noted that at a given time in the reduction process the particle size and the population of $(Pd)_n$ in

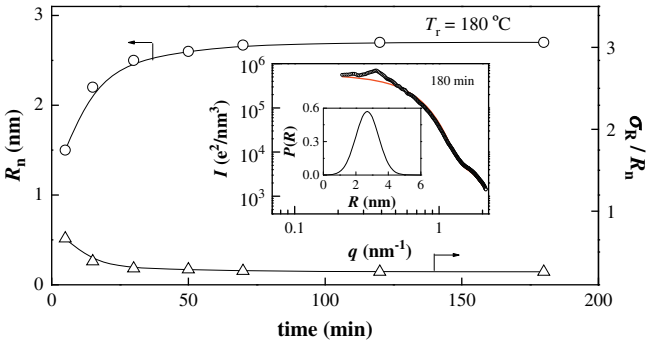

Fig. 6. Time dependence of characteristic parameters R_n and σ_R/R_n of $(Pd)_n$ formed at 180 °C. The inset shows both the measured scattering profile (symbols) and the best-fitted theoretical profile (red line) after the reduction at 180 °C for 180 min. The normalized distribution function of the particle size $P(R)$ in the same reduction condition is also given. (For interpretation of colour in this figure, the reader is referred to the web version of this article.)

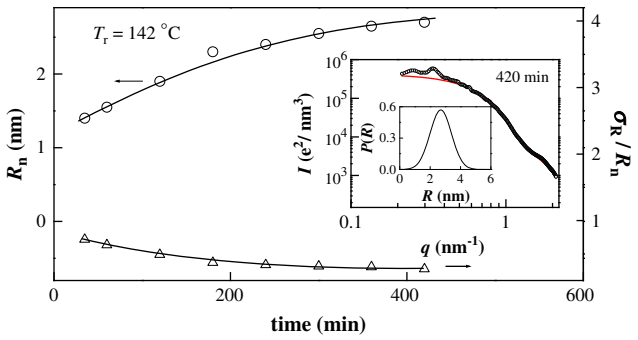

Fig. 7. Time dependence of characteristic parameters R_n and σ_R/R_n of $(Pd)_n$ formed at 142 °C. The inset shows both the measured scattering profile (symbols) and the best-fitted theoretical profile (red line) after the reduction at 142 °C for 420 min. The normalized distribution function of the particle size $P(R)$ in the same reduction condition is also given. (For interpretation of colour in this figure, the reader is referred to the web version of this article.)

the PS and PI lamellae are not the same because the kinetics of the reduction and that of the growth of $(Pd)_n$ are different in the two lamellae. However, these effects do not affect our analysis of $(Pd)_n$ particles at all, because our analysis based on the independent scattering theory includes the particles in the both lamellae.

We plotted R_n vs time for both samples on a double-logarithmic scale in Fig. 8a and b, respectively. In addition to R_n, the weight-averaged radius of $(Pd)_n$ defined by

$$R_w = \frac{\int_0^\infty RP(R)R^3\,dR}{\int_0^\infty P(R)R^3\,dR} \quad (4)$$

was plotted in the same figures. Both R_n and R_w are approximated by the power law functions against time, though the relevant time span is not sufficiently long. In both cases, $R_n \sim t^n$, where n is close to 1/3, indicating the trend for the growth of $(Pd)_n$ via the diffusion and coalescence of $(Pd)_n$ clusters in the polymer matrix [46]. While $R_w \sim t^m$, where m is close to 0.15 and is much smaller than 1/3, indicating that large particles grow slower than small particles, since the contribution of large particles to R_w outweighs that of the small particles. The power law exponents at 180 °C are almost the same as those at 142 °C, implying a similar growth mechanism at different reduction temperatures, hence only the growth rate being different at these two temperatures.

If we define t_{end} as the time in which the reduction will be effectively finished, we have $t_{end,180} \sim 30$ min and $t_{end,142} \sim 350$ min for the reduction at 180 °C and 142 °C, respectively. Thus, the characteristic shift factor at a given temperature T relative to 142 °C, α_T, is defined by $\alpha_T = t_{end,142}/t_{end,T}$; $\alpha_{180} = t_{end,142}/t_{end,180} = 11.7$ at 180 °C and $\alpha_{142} = t_{end,142}/t_{end,142} = 1$ at 142 °C, respectively. Both R_n and R_w at the two temperatures are plotted against the reduced time, $t\alpha_T$, in Fig. 9a. The two curves superpose each other, indicating that although the reduction process at 180 °C is too fast to be accurately followed, the reduction details could be deduced from the reduction at lower temperatures (e.g., 142 °C) because of the same growth mechanism. Since both R_n and R_w are scaled with $t\alpha_T$, σ_R/R_n is expected to be also scaled naturally with $t\alpha_T$. The plot of σ_R/R_n as a function of $t\alpha_T$ in Fig. 9b shows a master curve independent of T_r, verifying this expectation.

It is interesting to note that there is a critical particle size, $R_{n,c}$ or $R_{w,c}$, above which the particle growth is pinned ($R_{n,c} \cong 3$ nm) and that this critical size is independent of T_r. We believe that this is due

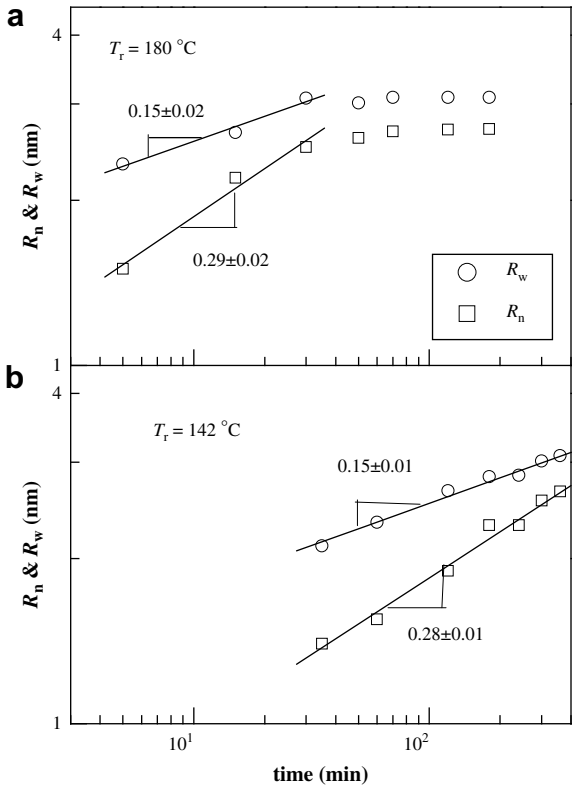

Fig. 8. Time dependence of R_n and R_w of $(Pd)_n$ formed at (a) 180 °C and (b) 142 °C.

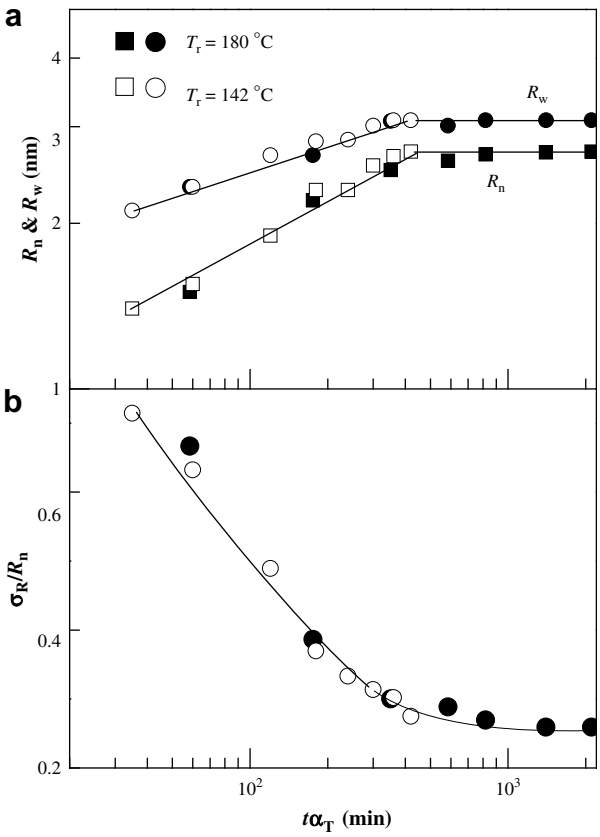

Fig. 9. (a) Reduced-time dependence of R_n and R_w at 180 °C and 142 °C. (b) Reduced-time dependence of σ_R/R_n at 180 °C and 142 °C. α_T is the shift factor with respect to the reference temperature 142 °C.

to the suppressed Brownian motion of $(Pd)_n$ particles in the viscoelastic polymer matrix: As R_n or R_w of $(Pd)_n$ increases toward the radius of gyration R_g of the bcp ($R_g \cong 4.3$ nm), the particles will encounter increasing viscoelastic drags in the bcp matrix and be eventually trapped in the bcp matrix, which will pin down the growth of the particles mediated by the particle–particle coalescence and the welding into a larger particle. A further growth of the particles may occur via absorption of reduced atoms, if there are sufficient $Pd(acac)_2$ remaining. However, the fractional growth rate $(1/R_n)dR_n/dt$ will be very small when R_n is ~3 nm. The decrease of the fractional growth rate with t as well as the existence of the critical size may explain themselves the decrease of σ_R/R_n.

If inter-sphere interference of scattering waves from $(Pd)_n$ is negligible (i.e., in the independent scattering criterion), the scattered intensity per unit volume of the systems composed of $(Pd)_n$ spheres is given by:

$$I(q) = \frac{N_p\overline{I_{sph}(q)}}{V_t} = \rho_0^2\left(\frac{N_p v_w^2}{V_t}\right)\left[\frac{\overline{v^2F(q)}}{v_w^2}\right] = \rho_0^2\phi_p v_w\left[\frac{\overline{v^2F(q)}}{v_w^2}\right] \quad (5)$$

where N_p is the total particle number, v_w is the weight-averaged volume of the spheres, V_t is the total irradiated volume of the system, and ϕ_p is the volume concentration of the spheres, defined by $\phi_P \equiv N_P v_w/V_t$, Therefore,

$$I(q)v_w^{-1} = K\phi_p\left[\frac{\overline{v^2F(q)}}{v_w^2}\right] \equiv K\phi_p\Phi(q) \quad (6)$$

where K $(\equiv\rho_0^2)$ is the proportionality constant and $\Phi(q) \equiv [\overline{v^2F(q)}/v_w^2]$.

Fig. 10a and b shows the reduced scattering intensity $I(qR_w)R_w^3$ vs the magnitude of reduced scattering vector qR_w with t at 180 °C and 142 °C, respectively, obtained from the time evolution of the scattering profiles shown in Figs. 4 and 5, respectively. The reduced intensity increases with increasing time for both cases. Moreover, a series of the reduced profiles obtained at different times have the same qR_w dependence at $qR_w > 1.2$, where the independent scattering approximation is valid. Hence they are superposable each other upon a vertical shift only. If this is the case, one can obtain the reduced scattering profile, $\Phi(qR_w)$, universal with the reduction time,

$$\Phi(qR_w) = I(qR_w)\frac{R_w^{-3}}{K\phi_P(t)} \quad (7)$$

as will be demonstrated later by Figs. 12 and 13. The amount of the vertical shift depends on the time evolution of the particle concentration $\phi_P(t)$.

In Fig. 11, we plot the relative concentration as determined from the vertical shift described above, $K\phi_P(t)$, vs time. Obviously, the rate of the "relative" concentration increase of $(Pd)_n$ depends on temperature. At 180 °C, the concentration of the $(Pd)_n$ at a given time is higher than that at 142 °C. By reducing $K\phi_P(t)$ further with the value at the final stage, $K\phi_{P,\infty}$, we calculated the kinetics of the particle concentration:

$$\frac{\phi_P(t)}{\phi_{P,\infty}} = \frac{\left(IR_w^{-3}\right)_t}{\left(IR_w^{-3}\right)_\infty} \quad (8)$$

The data on $\phi_P(t)/\phi_{P,\infty}$ at the two T_rs (shown by symbols) can be well fitted by the simple equation given below (solid lines in Fig. 11)

$$\phi_P(t) = \phi_{P,\infty}[1 - \exp(-kt)] \quad (9)$$

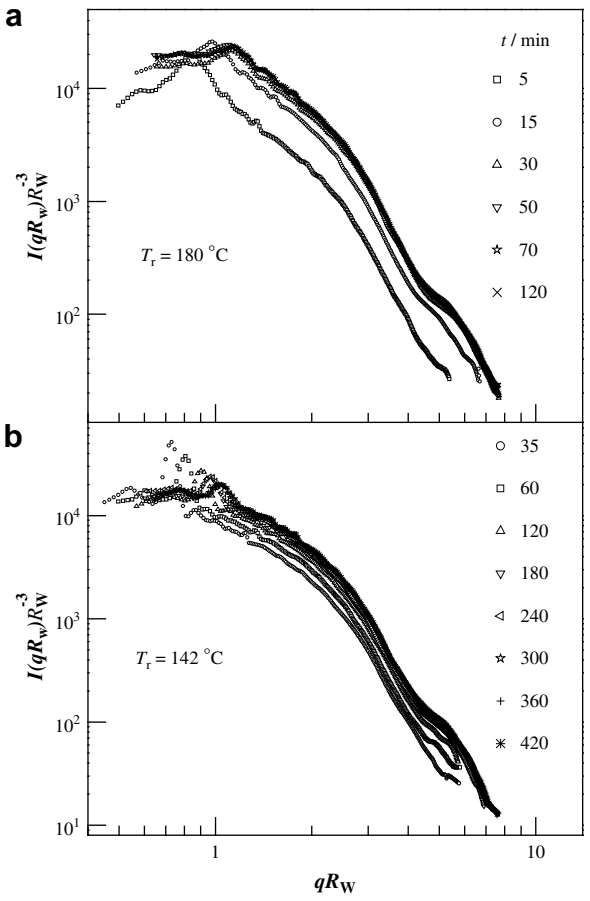

Fig. 10. Time dependence of the reduced scattering intensity $I(qR_w)R_w^{-3}$ vs the magnitude of reduced scattering vector qR_w at (a) 180 °C and (b) 142 °C. The numbers attached to the markers denote the reaction time in minutes.

where k is the temperature-dependent rate constant, $k = 0.068\ \mathrm{min}^{-1}$ and $0.0115\ \mathrm{min}^{-1}$ at $T = 180$ °C and 142 °C, respectively, for the first-order reaction, as will be shown below.

Here an essential part of the thermal reduction reaction of $Pd(acac)_2$ may be given by

$$\mathrm{Pd(II)} + 2\mathrm{e}^- \rightarrow \mathrm{Pd(0)} \tag{10}$$

and the formation of $(Pd)_n$ composed of number of Pd(0) atoms defined by n is given by

$$n\mathrm{Pd(0)} \rightarrow (\mathrm{Pd})_n \tag{11}$$

with the assumption of the concentration $\phi_P(t)$ of $(Pd)_n$ at a given time t being proportional to the concentration of the total reduced Pd(0) atoms, $[Pd(0)]_t$, up to the reduction time t. Note that

$$\frac{\phi_P(t)}{\phi_{P,\infty}} = \frac{[\mathrm{Pd(0)}]_t}{[\mathrm{Pd(0)}]_\infty} = \frac{\{[\mathrm{Pd(II)}]_0 - [\mathrm{Pd(II)}]_t\}}{[\mathrm{Pd(II)}]_0} \tag{12}$$

and that from Eq. (10),

$$-\frac{\mathrm{d}}{\mathrm{d}t}[\mathrm{Pd(II)}] = k[\mathrm{Pd(II)}] \tag{13a}$$

so that

$$[\mathrm{Pd(II)}]_t = [\mathrm{Pd(II)}]_0 \exp(-kt) \tag{13b}$$

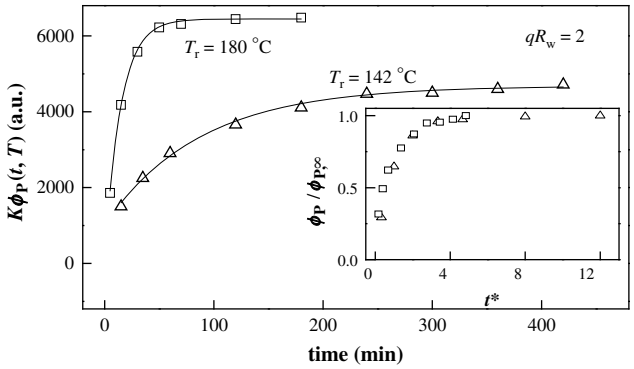

Fig. 11. Time dependence of the relative concentration of $(Pd)_n$, $K\phi_P(t, T)$. The inset shows the plot of $\phi_P/\phi_{P,\infty}$ against the reduced time t^*.

From Eqs. (12) and (13b), we obtain Eq. (9). Here $[Pd(II)]_t$ is the concentration of Pd(II) ions at time t, while $[Pd(0)]_\infty$ is the total concentration of Pd(0) atoms reduced during the whole reduction process. $[Pd(II)]_0$ is the initial concentration of Pd(II) ions. We assume that all the Pd(II) ions can be reduced to Pd(0) atoms at 180 °C. Thus the reducible Pd(II) ions at 142 °C are ~70%, which is estimated from the saturation level of $\phi_{P,\infty}$ shown in Fig. 11. We note that Eq. (13) is derived on the basis of the first-order reaction in Eq. (10).

If we define the characteristic time, τ, as $\tau = 1/k$, and plot $\phi_P(t)/\phi_{P,\infty}$ against the reduced time $t^* = t/\tau$, a master curve universal with the reduction temperature was obtained as shown in the inset of Fig. 11, revealing that the reduction mechanism is independent of T and hence of the segregation states of PS and PI segments in the reaction matrix.

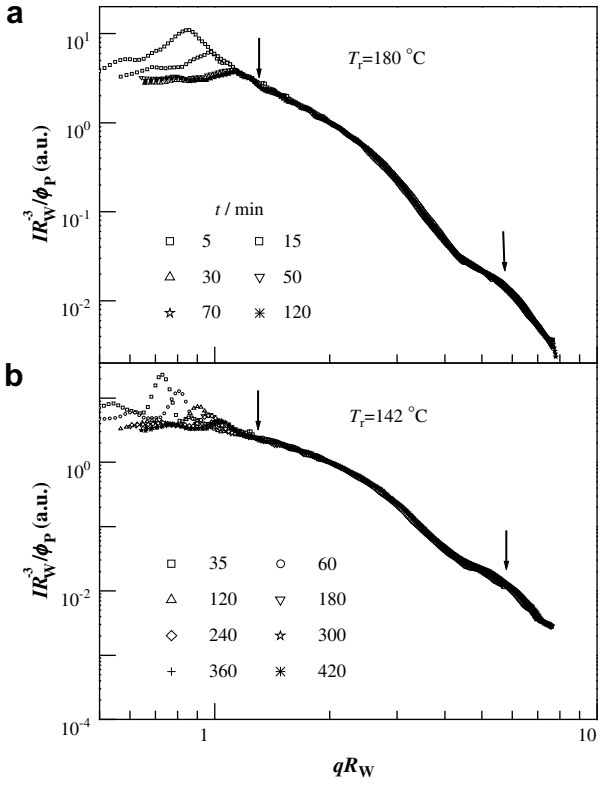

Fig. 12. Time dependence of a reduced plot of IR_w^3/ϕ_P vs qR_w at (a) 180 °C and (b) 142 °C. The arrow marked at $qR_w \sim 1.2$ indicates the limiting value of qR_w, above which the assumption for the independent scattering from $(Pd)_n$ is valid. The arrow marked at $qR_w \sim 5.7$ shows a peak or shoulder of the form factor of $(Pd)_n$ spheres. The numbers attached to the markers denote the reaction time in minutes.

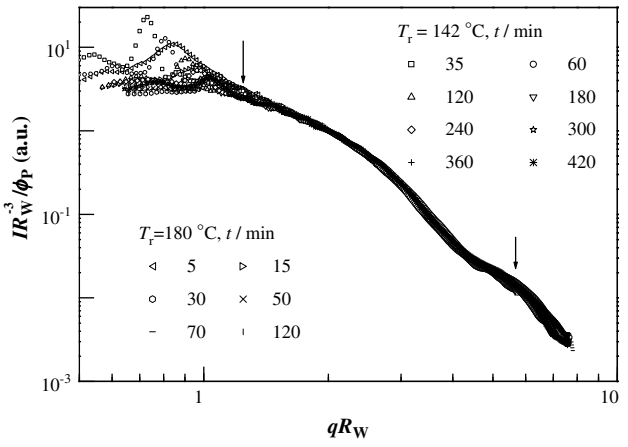

Fig. 13. Reduced plot of IR_w^3/ϕ_P vs qR_w at both 180 °C and 142 °C plotted on the same graph, indicating that the two master curves obtained at these temperatures superpose well one another. The numbers attached to the markers denote the reaction time in minutes. The arrows have the same meaning as those in Fig. 12.

Fig. 12 shows a reduced plot of IR_w^{-3}/ϕ_P vs qR_w. All the reduced intensity profiles obtained at varying times at a given temperature were superposed one another at $qR_w \geq 1.2$, indicating validity of the following relationship,

$$I(qR_w, t)R_w^{-3} = K\phi_P(t)\Phi(qR_w) \quad (14)$$

for $qR_w \geq 1.2$, where the criterion for the independent scattering of $(Pd)_n$ is valid. Thus $\Phi(qR_w)$ at $qR_w \geq 1.2$ represents the scaled form factor of $(Pd)_n$ formed at the given temperature, either at 180 °C or 142 °C, which is universal with the reduction time [47]. The universal scaled form factor of $(Pd)_n$ at the given temperature is found to be obtained by reducing the scattered intensity with the time- and temperature-dependent averaged particle volume $R_w(t, T)^3$ and particle concentration $\phi_P(t, T)$ and by reducing q with $R_w(t, T)^{-1}$. The arrow at $qR_w \sim 5.7$ corresponds with the first-order peak or shoulder of the form factor of spheres. The non-universality found in $\Phi(qR_w)$ at $qR_w \leq 1.2$ is due to a break down of the criterion for the independent scattering approximation. In this q region the scattering depends on interparticle interference of scattering waves from the particles and hence on a time-dependent spatial distribution of the particles. Hence the scattering cannot be scaled with the parameters $R_w(t, T)$ and $\phi_P(t, T)$ characterizing the individual particles only.

The scaled form factors $\Phi(qR_w)$ at $qR_w \geq 1.2$ obtained at 180 °C and 142 °C turned out to be identical within the experimental accuracy as demonstrated in Fig. 13. The figure verifies that the $\Phi(qR_w)$s are superposed each other when they are plotted on the same reduced intensity scale and the reduced q scale. Consequently, we can elucidate that the scaled form factor is universal with temperature also [48]. Thus we can conclude that the reduction temperature does not affect the reduction mechanism of $Pd(acac)_2$ and the growth mechanism of $(Pd)_n$ and that it changes only the kinetics via $k(T)$ or $\phi_P(t, T)$ in Eq. (9) or $R_w(t, T)$ in Eq. (14). In other words, the thermal reduction of $Pd(acac)_2$ and growth of the $(Pd)_n$ in the disordered state and ordered state follow the same mechanisms.

5. Conclusion

We have succeeded in developing a nanocomposite composed of PS-*b*-PI symmetric block copolymer and the palladium nanoparticles, $(Pd)_n$, both in the ordered state and the disordered state where $(Pd)_n$ was created via thermal reduction of $Pd(acac)_2$, introduced in the as-cast PS-*b*-PI films, below and above the order–disorder transition temperature (for example at 142 and 180 °C, respectively). The reduction process of $(Pd)_n$ was studied *in situ* by the time-resolved SAXS measurements. Our results indicate that the reduction reaction from $Pd(acac)_2$ to Pd(0) atoms obeys the first-order kinetics in both the disordered and ordered PS-*b*-PI matrix. $Pd(acac)_2$ was first preferentially incorporated in PS lamellar microdomains in the as-cast film, indicating a stronger attraction between $Pd(acac)_2$ and PS blocks than that between $Pd(acac)_2$ and PI blocks. When the reduction starts to occur, the $(Pd)_n$ is created more rapidly in PI-rich regions than in the PS-rich regions for the reduction in the disordered state or in PI lamellar microdomains than in PS lamellar microdomains for the reduction in the ordered state. The higher reduction temperature ($T_r = 180$ °C) results in the larger reduction rate of $Pd(acac)_2$ and growth rate of $(Pd)_n$ than those at $T_r = 142$ °C, but the reduction and growth mechanism themselves are identical at these two temperatures and hence are independent of the reduction field (the ordered lamellar or disordered field). Moreover, these nanoparticles undergo ODT at different temperatures as will be reported in a companion paper [41].

References

[1] Park M, Harrison C, Chaikin PM, Register RA, Adamson DH. Science 1997;276:1401–4.
[2] Spatz JP, Eibeck P, Mossmer S, Möller M, Herzog T, Ziemann P. Adv Mater 1998;10:849–52.
[3] Hashimoto T, Fukunaga K. In: Zvelindosky AV, editor. Nanostructure soft matter. Springer; 2007. p. 45–97.
[4] Hamley IW. The physics of block copolymers. Oxford: Oxford University Press; 1998.
[5] Khandpur AK, Forster S, Bates FS, Hamley IW, Ryan AJ, Bras W, et al. Macromolecules 1995;28:8796–806.
[6] Sakamoto N, Hashimoto T. Macromolecules 1998;31:3292–302.
[7] Van Oene H. In: Polymer blends. Orlando: Academic Press; 1978.
[8] Fried JR. Polymer science and technology. Englewood Cliffs, NJ: Prentice-Hall Press; 1995.
[9] Usuki A, Kawasumi M, Kojima Y, Okada A, Kurauchi T, Kamigaito O. J Mater Res 1993;8:1174–8.
[10] Templin M, Frank A, Chesne AD, Leist H, Zhang Y, Ulrich R, et al. Science 1997;278:1795–8.
[11] Zhao D, Feng J, Huo Q, Melosh N, Fredrickson GH, Chmelka BF, et al. Science 1998;279:548–52.
[12] Thompson RB, Ginzburg VV, Matsen MW, Balazs AC. Science 2001;292:2469–72.
[13] Edrington AC, Urbas AM, DeRege P, Chen CX, Swager TM, Hadjichristidis N, et al. Adv Mater 2001;13:412–25.
[14] Lopes WA, Jaeger HM. Nature 2001;414:735–8.
[15] Fendler JH. Nanoparticles and nanostructured films. Weinheim: Wiley-VCH; 1998.
[16] Yue J, Sankaran V, Cohen RE, Schrock RR. J Am Chem Soc 1993;115:4409–10.
[17] Sankaran V, Yue J, Cohen RE, Schrock RR, Silbey R. J Chem Mater 1993;5:1133–42.
[18] Chan YNC, Schrock RR, Cohen RE. Chem Mater 1992;4:24–7.
[19] Chan YNC, Craig GSW, Schrock RR, Cohen RE. Chem Mater 1992;4:885–94.
[20] Saito R, Okamura S, Ishizu K. Polymer 1992;33:1099–101.
[21] Horiuchi S, Sarwar MI, Nakao Y. Adv Mater 2000;12:1507–11.
[22] Hashimoto T, Harada M, Sakamoto N. Macromolecules 1999;32:6867–70.
[23] Sakamoto N, Harada M, Hashimoto T. Macromolecules 2006;39:1116–24.
[24] Hashimoto T, Tsutsumi K, Funaki Y. Langmuire 1997;13:6869–72.
[25] Ribbe AE, Okamura A, Matsushige K, Hashimoto T. Macromolecules 2001;23:8239–45.
[26] Adachi M, Okumura A, Sivaniah E, Hashimoto T. Macromolecules 2006;39:7352–7.
[27] Seregina MV, Bronstein LM, Platonova OA, Chernyshov DM, Valetsky PM, Hartmann J, et al. Chem Mater 1997;9:923–31.
[28] Chan NgC, Graig GS, Schrock RR, Cohen RE. Chem Mater 1992;4:885–94.
[29] Ciebien JF, Cohen RE, Duran A. Supermol Sci 1998;5:31–9.
[30] Hashimoto T, Suehiro S, Shibayama M, Saijo K, Kawai H. Polym J 1981;13:501–16.
[31] Bates FS, Rosedale JH, Fredrickson GH. J Chem Phys 1990;92:6255–70.
[32] Stühn B, Mutter R, Albrecht T. Europhys Lett 1992;18:427–32.
[33] Wolff T, Burger C, Ruland W. Macromolecules 1993;26:1707–11.
[34] Hashimoto T, Ogawa T, Han CD. J Phys Soc Jpn 1994;63:2206–14.
[35] Floudas G, Pakula T, Fischer EW, Hadjichristidis N, Pispas S. Acta Polym 1994;45:176–81.
[36] Sakamoto N, Hashimoto T. Macromolecules 1995;28:6825–34.
[37] Fredrickson GH, Helfand E. J Chem Phys 1987;87:697–705.
[38] Koga T, Koga T, Hashimoto T. Phys Rev E 1999;60:R1154–7.
[39] Hashimoto T, Nagatoshi K, Todo A, Hasegawa H, Kawai H. Macromolecules 1974;7:364–73.

[40] Porod G. Kolloid-Zeitschrift 1951;124:83–114.
[41] Zhao Y, Saijo K, Takenaka M, Koizumi S, Hashimoto T. Macromolecules 2009.
[42] We first dissolved an equal amount of the homopolymers PS ($M_w \sim 12{,}000$) and PI ($M_w \sim 9000$) (4.95 wt%) and $Pd(acac)_2$ (0.05 wt%) in benzene, and put the resultant yellow solution into a very narrow glass tube. Then the evaporation of the solvent was allowed extremely slowly at room temperature for two months. The homopolymers PS and PI can be well phase-separated macroscopically after all the solvent slowly evaporated. Finally we obtained two clearly separated layers: a light yellow upper layer (PI phase) and a dark yellow bottom layer (PS phase). It implies that $Pd(acac)_2$ is preferentially incorporated in PS phase.
[43] It should be noted that $Pd(acac)_2$ and Pd(0) atoms have almost the same electron density, so that the preferential reduction in the PI-rich region in the disordered state or in the PI lamella in the ordered state alone does not bring about the change in electron density difference $\Delta\rho_{fluct.}$ or $\Delta\rho_{domain}$, respectively.
[44] Guinier A, Fournet G. Small-angle scattering of X-rays. NY: John Wiley & Sons; 1955.
[45] On the contrary to the case of Ref. [26], we should note that the system to be studied here does not have the bulk $Pd(acac)_2$ solution phase coexisting with the microdomains. Consequently process 2 in Fig. 7 of Ref. [26] does not exist. Nevertheless the diffusion and coalescence of Pd(0) atoms into $(Pd)_n$ (process 1) should occur in gaseous state of Pd(0) atoms as well as the Ostwald ripening or the Lifschitz–Slyozov–Wagner process (process 3a) and the diffusion–coalescence of $(Pd)_n$ into larger $(Pd)_n$ (process 3b) should occur in liquid state of $(Pd)_n$. Moreover, the growth of $(Pd)_n$ should occur by absorbing Pd(0) atoms.
[46] Binder K, Stauffer D. Phys Rev Lett 1974;33:1006–9.
[47] In a more rigorous sense, the size distribution of the nanoparticles depends on time, becoming smaller as the reduction progresses and R_w increasing. Consequently, the form factor cannot be rigorously scaled with a single length parameter of R_w, but depends on σ_R as well. This should result in small discrepancies in $\Phi(qR_w)$ at different reduction times. However, the change of σ_R with time is relatively small as shown in Figs. 6 and 7, so that the form factor is approximately scaled with the single length parameter R_w.
[48] A similar argument as given in Ref. [47] is also applied to the scaled form factor Φ (qR_w) universal with T. As σ_R depends on T also, Φ (qR_w) should depend on T as well. This should give rise to a discrepancy in the two scaled form factors obtained at $T = 142$ and 180 °C. However, the difference of σ_R at these two temperatures was small enough so that it did not bring about a significant discrepancy in the reduced plots employed in this figure.